

Copied by SANTOS Ltd.
for Rehmi Biever
on 2/7/98



SPE 36450

Microseismic Monitoring of the B-Sand Hydraulic Fracture Experiment at the DOE/GRI Multi-Site Project

N.R. Warpinski, SPE, Sandia Natl. Labs, and T.B. Wright, SPE, Resources Engineering Systems, and J.E. Uhl, B.P. Engler, and P.M. Drozda, Sandia Natl. Labs, and R.E. Peterson, SPE, and P.T. Branagan, SPE, Branagan & Assoc.

This paper was prepared for presentation at the 1996 SPE Annual Technical Conference and Exhibition held in Denver, Colorado, U.S.A. 6-9 October 1996

This paper was selected for presentation by an SPE Program Committee following review of information contained in an abstract submitted by the author(s). Contents of the paper as presented, have not been reviewed by the Society of Petroleum Engineers and are subject to correction by the author(s). The material, as presented, does not necessarily reflect any position of the Society of Petroleum Engineers, its officers, or members. Papers presented at SPE meetings are subject to publication review by Editorial Committees of the Society of Petroleum Engineers. Permission to copy is restricted to an abstract of not more than 300 words. Illustrations may not be copied. The abstract should contain conspicuous acknowledgment of where and by whom the paper was presented. Write Librarian, SPE, P.O. Box 833836, Richardson, TX 75083-3836, U.S.A. fax 01-214-952-9435

Abstract

Six hydraulic-fracture injections into a fluvial sandstone at a depth of 4500 ft were monitored with multi-level triaxial seismic receivers in two wells, resulting in maps of the growth and final geometry of each fracture based upon microseismic activity. These diagnostic images show that the hydraulic fractures are highly contained for smaller-volume KCl-water injections, but height growth is significant for the larger-volume, higher-rate, higher-viscosity treatments. Fracture lengths for most injections are similar. Final results are also compared with fracture models.

Introduction

The imaging of hydraulic fractures at depth has been a long-sought goal of the petroleum industry. Fracturing is an expensive, yet essential, element of production for many gas reservoirs and has significantly improved economics for many oil reservoirs as well. The Gas Research Institute and the US Department of Energy have long funded diagnostics programs and have achieved a slow but steady progress toward the realization of such technology. Fracture imaging is now attainable due to the improved capabilities of advanced receiver technology, advanced telemetry, and portable high-power computing. It is only characteristics of the reservoir and the well configurations which limit the potential of the technique. This paper describes the results of a series of fracturing experiments in a single reservoir interval that demonstrates the capabilities of this technology and its value

to related issues of modeling and fundamental model mechanisms.

Background

Fracture diagnostics have a long history that includes production history matching, post-frac well testing, radioactive tracers, temperature logs, pressure decline analysis, treatment pressure analysis and modeling, surface tiltmeters, surface electromagnetic techniques, and various seismic techniques. All of these diagnostics are indirect, in the sense that they measure some parameter associated with the hydraulic fracture and infer fracture characteristics from the parameter or its changes. As with most indirect techniques, problems with uniqueness and inversion abound.

One of these techniques is different, however, and is capable of producing a highly accurate image of the fracture without the processing difficulties inherent in inversion problems. The microseismic method,¹⁻⁶ one of several seismic technologies, is an indirect technique in that it monitors small faults or slippages that occur in the vicinity of the fracture (rather than the fracture itself), but is fully capable of producing an image of these microearthquakes. With proper interpretation models for the reservoir under consideration, the relation of the microseisms to the fracture can be clearly established. More importantly, for reservoirs with highly compressible fluids (e.g., gas reservoirs), the envelope of microseisms is approximately the same as the fracture size, with the exception of the width. Thus the microseismic method can produce relatively accurate images of the fracture length, height, and azimuth.

The microseismic technique is the primary diagnostic method employed to monitor fractures at the M-Site. It builds upon a technology proven in several elaborate field experiments,^{1,7-10} but with a focus of developing a viable, wireline-run, fracture-diagnostic service. As such, validation is an essential element of building confidence in this technology, and the M-Site experiments have been designed to provide that validation, particularly through the application of downhole inclinometers and intersecting wells.

In addition to improving fracture diagnostics, a secondary goal of the M-Site experiments has been to improve and validate fracture models and to better understand model mechanisms. This goal is accomplished by providing a site with well known properties, fully monitored fracture treatments, time-imaged fracture geometries, comparison of diagnostic results with various models, and even specialized fracture monitoring technology (as in an intersecting well) that can provide previously unavailable information.

M-Site

Details of the M-Site layout and fracture treatments have been given in a companion paper (Peterson et al.¹¹) and are only briefly repeated here. The M-Site field experiments, located at the previous Multiwell Experiment site in the Piceance basin of Colorado, are co-funded by the Gas Research Institute (GRI) and the US Department of Energy, and several additional contractors are funded directly by GRI. The reservoirs undergoing testing are fluvial Mesaverde sand-shale sequences, so the technologies developed in this difficult environment are easily translatable to many other reservoirs throughout the world. Details of previous work can be found in several papers and reports.⁹⁻¹²

A schematic of the well, instrument, and sandstone layout are shown in Figure 1. The site consists of one treatment well (MWX-2), one monitor well with cemented-in triaxial seismic receivers and bi-axial inclinometers and one cased observation well for wireline run tools (MWX-3). Not shown in the figure is an intersection well with deviated laterals for penetrating through the created hydraulic fractures in each sandstone.

The monitor well provides the instrumentation for validating the seismic results. Thirty triaxial receiver stations, with low-noise, wide-bandwidth accelerometers provide high quality microseismic data which can be accurately located. In the same well six bi-axial tiltmeters with nanoradian resolution provide information on the mechanical deformation of the formation which is used to validate the seismic results. The 7-in cased observation well is used for multi-level, wireline-run, triaxial receiver arrays, of the type that will be used in a commercial fracture diagnostic service. This array uses the same accelerometers as are grouted in the monitor well, and the multi-level feature also provides for highly accurate microseismic event location. The monitor well results, with many more levels to apply in location algorithms, are used to verify the data obtained from the wireline receiver arrays.

Additional information obtained in the treatment well, such as bottom-hole pressure, spectral gamma logs of radioactive tracer distributions, and seismic surveys, are used for detailed fracture modeling and additional diagnostic information. Detailed stress, rock property and reservoir property data are also available for these reservoirs and are used for fracture models, finite element deformation models,

and analyses of the mechanical response of the formation to the fracture treatment.

Additionally, crosswell seismic surveys were conducted to determine the p-wave and s-wave structure at the site. Seismic data were obtained with 5-ft source and receiver spacings in the treatment and monitor well, respectively, and the permanent 30-ft spacing of the cemented receivers in the monitor well. The seismic source was an airgun which provided excellent p-waves and generally good s waves. Both p and s tomograms have been produced, as well as Poisson's ratio and calculated uniaxial stress tomograms.

The lithology of the B sandstone is somewhat complicated by a second sand lobe that lies below the main 30 ft interval of the B sandstone. Figure 2 shows a gamma log of this configuration taken from the treatment well. The stress contrasts around the B sand, as determined from microfracture stress measurements, are shown in Figure 3. For modeling purposes, more detailed calibrated stress logs were also developed.

During B-sand testing, six different fracture injections using three different fluids were monitored. Important information on the injections are given in Table 1.

Table 1 Treatment Data

	FRACTURE	VOLUME (bbl)	FLUID	RATE (bpm)	SAND (LB)
2B	Step-Rate	27	KCl	0.5-3	
3B	Pump-In #1	100	KCl	10	
4B	Pump-In #2	210	KCl	10	
5B	Minifrac #1	400	40# Linear	22	
6B	Minifrac #2	400	40# Linear	22	
7B	Propped Frac	670	X-Link Gel	20	77,600

Receiver Orientation

Cemented-in receivers in the monitor well were oriented using three different techniques. During installation of the receivers, a radioactive pip was inserted in a known location on the receiver, and, subsequent to cementing, was located using a rotating gamma-ray logging tool. This orientation was confirmed using polarization data from perforations in the treatment well and from polarization of the crosswell survey data. With the exception of a couple of levels in which one or more receiver axes were clearly non-functioning, there was good agreement between the different orientation techniques.

Orientation of the five-level receiver system was accomplished by conducting an airgun orientation scan in the treatment well at 10-ft spacing over the interval in which microseisms were expected. Polarizations of p-wave arrivals for each level were analyzed to provide accurate orientation.

Microseismic Processing

Microseisms were processed in the standard manner, with p-wave arrivals, s-wave arrivals, and p-wave particle motion

detected on as many levels from each well as possible. Considerable automatic processing was performed to aid in initial analyses, but all results were quality checked by an analyst. Although advanced seismic analyses are in progress (using Nelson and Vidale's algorithms^{13,14}), initial seismic results using simpler techniques have been found to be quite accurate because of the large number of receiver stations.

The initial results assume a single p-wave velocity and a single velocity factor, given by

$$V_f = \frac{V_p V_s}{V_p - V_s} \quad (1)$$

which is used to calculate the distance to a microseism based on the arrival time separation of the p and s waves,⁹ given by

$$d = V_f(t_s - t_p) \quad (2)$$

where t_s is the s-wave arrival time and t_p is the p-wave arrival time. The distance and elevation of the microseism are first calculated using a regression analysis on the ray-path travel times to all of the receiver stations at which a p-wave arrival has been determined. Uncertainty analysis of the results shows that such a calculation is highly accurate for the elevation (because of the large number of vertically arrayed receivers), but has considerable error in the distance (because all of the receivers are vertically arrayed). To improve on the distance calculation, p-s separations are found wherever possible and the average distance to the microseism are reduced. The orientation of the microseism in the horizontal plane is calculated by averaging all of the levels in which the orientation of the p-wave particle motion is accurate (usually 8-10 levels for the monitor well and 3-4 levels for the five-level wireline array). Given the distance, elevation and orientation, microseismic points can be mapped. As noted earlier, more advanced analyses are in progress, but initial comparisons show little difference in the two results.

Figure 4 shows an example microseism detected on the monitor-well array across 17 levels. In this typical example, the p-wave arrival is discernible on nearly every level (a few levels have non-functioning accelerometers) and s-wave arrivals are evident on many of the upper and lower levels. Given such detailed data, accurate locations for most microseisms are routine. One exception to the height accuracy occurred during the initial injections using KCl water. During these tests only a single receiver was used in MWX-3 and elevation locations from a single receiver are notoriously inaccurate because the velocity structure of the formation results in bent ray-paths and misleading vertical locations. To avoid misleading data for fracture height, all single receiver data were scaled back to fit within the height determined by the full array of monitor-well receivers for the same injection. Thus, height on these tests was only determined by monitor well instrumentation and the single-level data should only be used for length and azimuth

information. With the minifracs and propped fracture treatment, the five-level array in MWX-3 was fully capable of providing accurate height data and no such scaling was needed for the later tests.

Microseismic locations are not necessarily on the hydraulic fracture, but can in fact be some distance to the side or even ahead of the fracture.¹⁵ Calculations of the mechanical response of the formation for B-sand conditions have been performed to estimate the zone of microseismic activity anticipated for this interval. These analyses show that microseismic events at this site can occur as much as 12-15 ft ahead of the tip of the fracture and 15-20 ft normal to the tip of the fracture because of the large stress concentrations at the fracture tip, and several tens of feet normal to the body of the fracture due to leakoff effects (increase in pore pressure). The exact distance at which leakoff-induced microseisms might occur is difficult to deduce because of unknown permeability of the natural fractures in the formation. Nevertheless, these analyses provide guidance in interpreting the microseismic data and show that the microseisms map out an envelope in which the hydraulic fracture is embedded. By examining this envelope, the height, length and azimuth of the fracture can be fairly accurately estimated, but nothing can be inferred about the width of the fracture or the number of fracture strands or width of any complex fracture zone that may or may not exist.

Fracture Diagnostic Results

Fracture diagnostic results are presented as plan views and side views of the microseismic locations. Given the geometry of the arrays, the most accurate position is the elevation of the microseism (because of the large number of receivers in vertical arrays), while the distance from the microseism to the receiver and the azimuth of the microseismic signal have more uncertainty. Accuracy of the elevation position is about ± 5 ft, but results vary from microseism to microseism depending on how many receivers have detected the particular event. Accuracy of the azimuth to the microseism is about $\pm 5^\circ$, and since the distance away is approximately 300 ft, the uncertainty in the azimuthal location is about 25 ft at that 300-ft distance. Uncertainty in the distance from the receiver to the microseism varies considerably depending upon the number of levels on which the s-wave arrival is accurately detected, but it is on the order of ± 50 ft.

Given the uncertainties in locations and the interpretation of microseisms discussed in the previous section, the microseismic results should be considered an envelope which surrounds the fracture. Furthermore, since uncertainties on a few microseisms can become relatively large, the position of any single outlier microseism should always be questioned.

Step Rate Test (2B). Figure 5 shows the final microseismic images of the 27 bbl step-rate test (maximum rate of 3 bpm),

with the side view image having an exaggerated vertical scale. This image suggests that the fracture is well contained within the upper part of the B sandstone and has a length of 150-200 ft. There also appears to be a slight asymmetry, with greater fracture length on the west wing. The plan view picture also shows that microseisms provide an envelope that surrounds the true fracture geometry. The exact position of any one microseism itself is unimportant and may be misleading. The boundaries of the B sandstone, as shown in the side view of Figure 5, are the top of the clean 30-ft section and the bottom of the thin sand lying beneath the clean section (see Figure 2).

Pump-In/Shut-In #1 (3B). Figure 6 shows the microseismic images of the first pump-in/shut-in test, which was conducted with approximately 100 bbl of KCl water pumped at 10 bpm. These images also show a fracture that is probably well contained. The single microseism below the B sandstone could easily be a point that is in error or a plane of weakness in the formation that is very favorably oriented for slippage to occur with minimal stress loading (microseisms can occur ahead of the fracture tip due to the large stress changes at and ahead of the tip of a fracture). Net pressures were about 900 psi during at shut-in (and climbing continuously during this treatment) compared to stress contrasts of about 1500 psi, so full containment is realistic and expected. It would also appear that the fracture is mostly in the thick upper 30 ft of the B sand. The average length of this fracture is on the order of 300 ft, with the east wing possibly being greater than the west wing of the fracture.

Pump-In/Shut-In #2 (4B). Figure 7 shows the microseismic images of the second 10-bpm, KCl-water, pump-in/shut-in test. This injection shows considerable asymmetry, with the west wing appearing to be about 300 ft and the east wing at least 400 ft. There is also indications that the volume of this test was sufficient to cause the fracture to at least begin breaking into the overlying layers. Net pressures during this treatment were about 1000 psi above closure stress at shut in (and climbing slightly). It is interesting to observe that there are often a few spurious microseismic event locations and they tend to be in similar locations of spurious events seen in other injections. Such results could be due to errors, but more likely there is some feature in the formation that is easily disturbed by the stresses induced by the hydraulic fracture. The timing of fracture growth was somewhat unusual because the fracture grew rather symmetrically during most of the treatment, but a surface leak resulted in an 8 minute shut down during the test. After this shutdown, the remaining approximately 60 bbls were injected and length growth was observed only on the east wing, resulting in the final asymmetric shape.

Minifrac #1 (5B). The microseismic image maps for the first minifrac (linear gel), injected at 22 bpm, are shown in Figure 8. In this injection the net pressure reached 1300 psi at shut in (and was relatively flat), close to the confining stress contrast of 1500 psi. Height growth is clearly evident in the microseismic data, with considerably more height growth occurring upward than downward. This fracture appears to have about the same length dimensions and the same asymmetry as the previous KCl injection, even though both the rate and volumes were doubled. Much of the volume was undoubtedly taken up in height growth and wider fracture widths on account of height growth. Indications of height growth appear early in the treatment, so the occurrence of height growth is due to rate or viscosity rather than volume, although the larger volume pumped results in additional height. It should be noted that there is one outlier on the east wing of the fracture that probably should be ignored

Minifrac #2 (6B). The second minifrac, which was pumped identically to the first minifrac, resulted in very similar pressure and microseismic images, as seen in Figure 9. There is again evidence of upward fracture growth and only limited evidence of any downward growth. The fracture is asymmetric, with a 300-ft west wing and an approximately 400-ft east wing. In this injection, the microseisms are very tightly banded around the fracture with no obvious outliers, whereas in several previous tests there was wide scatter of the microseisms. Reasons for such differences are unknown.

Propped Fracture Treatment (7B). The microseismic images from the propped fracture treatment are shown in Figure 10. During this 20-bpm injection, large amounts of upward height growth occurred, but all of it happened in the last one third of the treatment. During the first two thirds of the treatment, the fracture height looked very similar to the minifrac. Net fracture pressures reached 2000 psi during this treatment, but most of the excess over the minifrac (1300 psi net pressure) occurred after higher concentration sand hit the formation, possibly indicating that some form of proppant bridging may have induced the high pressures. Fracture length is relatively symmetric, with somewhat less than 400 ft of length observed on each wing (at least within the B sandstone). Two outliers suggest that the fracture may have grown up out of zone on the far end of the east wing, but there is too sparse of data to confirm this trend. Nevertheless, this treatment is entirely different than the previous injections and shows that fracture treatments with normal fracture fluids can induce height growth in high stress contrast environments.

Model Comparison

Comparisons of the microseismic images were made with two

models, FRACPRO¹⁶ and a conventional pseudo-3D simulator. FRACPRO was run in its standard mode with no additional features turned on. The FRACPRO model results were made at the site during the treatments, so there were no comparisons with microseismic data at that time to bias the results. The conventional pseudo-3D simulator is a straightforward equilibrium-height (with constraints) finite-difference model with enhanced wall roughness. This model was run until the FRACPRO-derived efficiency was matched. In both cases, the net pressure was matched, *except in the propped fracture treatment*. The propped fracture achieved very high net pressures late in the injection (2000 psi) after higher concentrations of sand were entering the formation, and no attempt was made to match the final pressure. More detailed model comparisons of these results will be presented in later papers.

Model comparison for three of the injections are shown in Figures 11-13 at a less exaggerated length scale. The 200 bbl pump-in/shut-in test data are given in Figure 11, the second minifrac data are shown in Figure 12, and the propped fracture treatment results are plotted in Figure 13. Results are quite interesting in that they show that models do a relatively good job of matching results when the fracture is well contained, but some problems arise when height growth occurs. For the water frac, FRACPRO has a somewhat smaller length and greater height than the imaged fracture, and the pseudo-3D model has considerably greater length.

For the 400-bbl minifrac, the situation is similar to the water injection, except that both models predict more height growth than actually imaged. Length results are relatively close, but the asymmetry skews the match.

For the propped frac, shown in Figure 13, the comparison is not very good and suggests that some features of the formation or the behavior of the fracture in this formation are not well understood. It is particularly difficult to account for the lack of downward growth. Stresses in the bounding layers are already modeled as greater than 1.0 psi/ft, so higher stresses in these layers are not reasonable.¹⁷ There must either be some other containment feature available, or the proppant has played a large role in minimizing downward growth. However, some downward growth was also expected for the minifrac, but was not observed, so the complete answer is probably more complicated. One other possibility is the microseismic event character is different in the lower shales and any microseisms are not detected, but this explanation requires that the shales above the B sand be different from the shales below, which is not observed. The total dimensions of the modeled fractures should not be taken as accurate results, because there was no match of net pressure using either of the models. As a result, the comparison between the two models may not be accurate. As indicators of general trends, however, these model runs show the difficulty with fracture height and the differences between different models.

Discussion and Conclusions

These results show that microseismic imaging techniques can be used to map out important features of hydraulic fractures in typical oil-field environments. The accuracy of microseismic imaging is sufficient to provide accurate estimates of the length, height and azimuth of a hydraulic fracture. However, accurate height determination requires multi-level receiver systems in order to account for formation layering. Table 2 gives an estimated size comparison for the six different injections.

Table 2 Comparison of Fracture Geometries

	AZIMUTH (deg)	HEIGHT (ft)	LENGTH (ft)
2B	N76W	40	175
3B	N74W	55	300
4B	N77W	55	350
5B	N74W	80	325
6B	N74W	75	350
7B	N74W	135	350

One comparison of the accuracy and reliability of the measurements that can be made from this set of experiments is the azimuth for each test. The azimuth listed on each plan view is that obtained only from the monitor well data (only the monitor well data are used because the instrumentation in MWX-3 changed during the testing from a single receiver during the water injections to a five-level system for later treatments and any comparison would be irrelevant). The average azimuth of the six tests is N75°W with a standard deviation of about 1°. The actual azimuth, based on the location of the fracture in an intersecting well is N72°W.¹⁸ Also, the azimuths using all data (both monitor and MWX-3) differ by as much as 2-3° from those given in Table 2.

The fracture length variations are interesting, because the length changes only slightly as the test progress from small volumes of low-viscosity fluids pumped at low rates to larger volumes of high-viscosity fluids pumped at high rates. Of course, the volume is taken up by the height growth induced by the higher net pressures in the latter treatments.

The degree of containment during the KCl injections is quite good, but the containment is only effective for small volumes of low viscosity fluid pumped at low rates. Under typical treatment conditions (fluids, volumes, rates), height growth occurred relatively easily and much fluid was lost treating out-of-zone rocks. Since the M-Site location is not likely to be different from other western basins, the high stress contrasts measured here which provided the initial containment may be prevalent throughout these areas. A good strategy for gas producers in these areas would be to work on techniques for fracturing these zones in ways which prolong the containment of the fracture.

Comparisons with other diagnostics^{18,19} were also made. Tracers in the treatment well showed no out-of-zone fracturing for the KCl injections and only about 20 ft of

growth for the minifrac, which is in good agreement with the microseismic results. However, there was significant disagreement in the propped fracture, where the tracers did not show evidence of any more height than seen in the minifrac. Filimeters¹⁹ gave direct evidence of the mechanical height of the fracture, yielding values of about 53 ft for the KCl injections and 67 ft for the minifrac. The propped fracture treatment had a geometry that was too complicated to produce a single height value, but the geometry imaged by the microseisms was shown to be able to produce the measured tilts.

Comparisons of fracture models with the imaged results were quite good for cases where the fracture was contained, but some discrepancies developed for the latter treatments. Of particular significance was the lack of downward growth, as it suggests that there may be other containment features which are not included in current models (i.e., inefficiency crossing bedding). Such features can be included in an *ad hoc* manner after the fact using features such as a slip condition or a limit on height growth, but they are not usually known beforehand under normal fracturing conditions and are thus difficult to apply. Another possibility is incorrect stress data, but stresses great enough to provide such containment are unlikely.

Although this paper is not intended to be a model comparison, the modeling results again show the differences typical of available models. Models such as FRACPRO provide for more height and less length than conventional pseudo-3D simulators and neither of them exactly match the imaged data because of a lack of information on all of the formation and reservoir features which may be important for this treatment. Even with the vast amount of data available at M-Site, it is difficult to obtain accurate model matches without using effects such as multiple fractures, tortuosity, fracture roughness, perfect slip, etc. The situation is much more uncertain in a typical oil-field environment where essentially no stress, modulus, or fracture complexity data are available.

Acknowledgments

The authors would like to acknowledge the Gas Research Institute, with funding for this project managed by Steve Wolhart, and the Department of Energy, with funding managed by Karl-H. Frohne, for their continued support of this project. Special thanks are in order for many contributors to this work at Sandia National Labs, Branagan & Associates, Resource Engineering Systems, CER Corporation, Jim Fix & Associates, Bolt Technology Corporation, and many others.

References

1. Albright, J.N. and Pearson, C.F., "Acoustic Emissions as a Tool for Hydraulic Fracture Location: Experience at the Fenton Hill Hot Dry Rock Site." *SPEJ*, August 1982, 523.
2. Lacy, I.L., "Comparison of Hydraulic Fracture Orientation Techniques," paper SPE 13225, proc., SPE Annual Tech. Conf.

- and Exh., Houston, TX, Sept. 16-19, 1984.
3. Dobecki, T. L., "Hydraulic Fracture Orientation Using Passive Borehole Seismics," SPE 12110, proc., Annual Tech. Conf. and Exh. of SPE, San Francisco, CA, Oct. 5-8, 1983.
4. Thorne, B.J. and Morris, H.E., "Advances in Borehole Seismic Fracture Diagnostics," SPE 16405, proc., SPE Symp. on Low Permeability Reservoirs, Denver, Co., May 18-19, 1987, 165.
5. Sarda, J-P., Perreau, P.J. and Deflandre, J-P., "Acoustic Emission Interpretation for Estimating Hydraulic Fracture Extent, paper SPE 17723, proc., Gas Tech. Symp., Dallas, TX, June 13-15, 1988, 183.
6. Stewart, L., Cassell, B.R. and Bol, G.M., "Acoustic Emission Monitoring During Hydraulic Fracturing," *SPE Formation Evaluation*, Vol. 7, June 1992, 139.
7. Vinegar, H.J. et al., "Active and Passive Seismic Imaging of a Hydraulic Fracture in Diatomite," *JPT*, Jan. 1992, 28.
8. Truby, L.S., Keck, R.G. and Withers, R.J., "Data Gathering for a Comprehensive Hydraulic Fracture Diagnostic Project: A Case Study," paper SPE 27506, proc., 1994 IADC/SPE Drilling Conf., Dallas, TX, Feb. 15-18.
9. Sleaf, G.E., Warpinski, N.R. and Engler, B.P., "The Use of Broadband Microseisms for Hydraulic Fracture Mapping," *SPE Form Eval.*, Dec. 1995, 233-239.
10. Middlebrook, M., Peterson, R., Warpinski, N.R., Engler, B., Sleaf, G., Cleary, M., Wright, T. and Branagan, P., "Multi-Site Project Seismic Verification Experiment and Assessment of Site Suitability," GRI Topical Report, GRI-93/0050, Feb. 1993.
11. Peterson, R.E., Wolhart, S.L., Frohne, K.-H., Warpinski, N.R., Branagan, P.T. and Wright, T.B., "Fracture Diagnostics Research at the GRI/DOE Multi-Site Project: Overview of the Concept and Results," SPE 36449, proc., SPE Annual Tech. Conf. and Exh., Denver, CO, Oct. 6-9, 1996.
12. Peterson, R. et al. "Results of Multi-Sites Experimentation in the A Sand Interval: Fracture Diagnostics, Fracture Modeling and Crosswell Tomography," GRI Topical Report, GRI-95/0066, April 1995.
13. Nelson, G.D. and Vidale, J.E., "Earthquake Locations by 3D Finite Difference Travel Times," *Bull. of the Seismological Society of America*, **80**, April 1990, 395.
14. Vidale, J.E., "Finite Difference Calculation of Travel Times," *Bull. of the Seismological Society of America*, **78**, 1988, 2062.
15. Warpinski, N.R., "Interpretation of Hydraulic Fracture Mapping Experiments," paper SPE 27985, proc., Tulsa Centennial Petroleum Engineering Symp., Tulsa, OK, Aug. 1994, 291.
16. Crockett, A.R., Willis, R.M. and Cleary, M.P., "Improvement of Hydraulic Fracture Predictions by Real-Time History Matching on Observed Pressures," *SPE Prod Eng.*, **4**, Nov. 1989, 408.
17. Warpinski, N.R. and Teufel, L.W., "In Situ Stresses in Low-Permeability Nonmarine Rocks," *JPT*, April 1989, 405.
18. Branagan, P.T., Peterson, R., Warpinski, N.R. and Wright, T.B., "The Characterization of Remotely Intersected Set of Hydraulic Fractures: Results of Intersection Well No. 1: GRI/DOE Multi-Site Project," SPE 36452, SPE Annual Tech. Conf. & Exh., Denver, CO, Oct. 6-9, 1996.
19. Branagan, P.T., Warpinski, N.R., Engler, B.P., Wilmer, R., "Measuring the Hydraulic Fracture-Induced Deformation of Reservoir and Adjacent Rocks Employing a Deeply Buried Inclinometer Array: GRI/DOE Multi-Site Project," SPE 36451, SPE Annual Tech. Conf. & Exh., Denver, CO, Oct. 6-9, 1996.

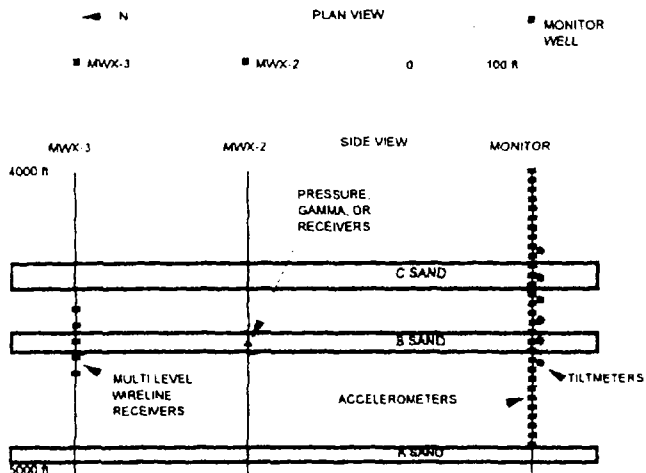


Figure 1. Layout of M-Site wells and instrumentation

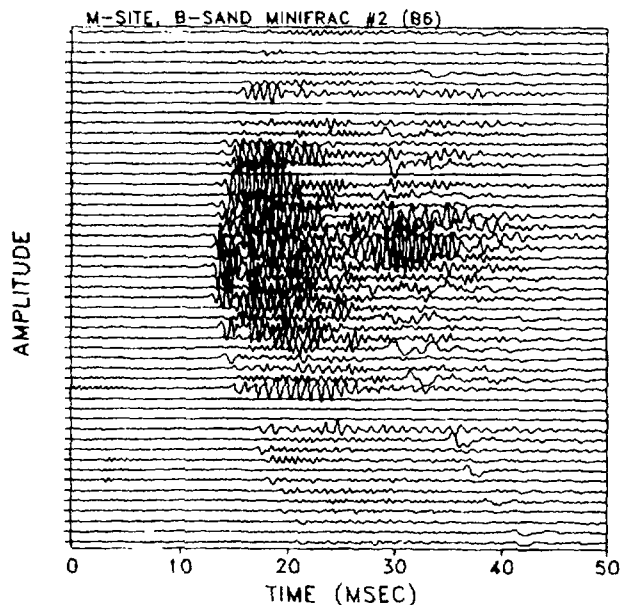


Figure 4. Example microseism

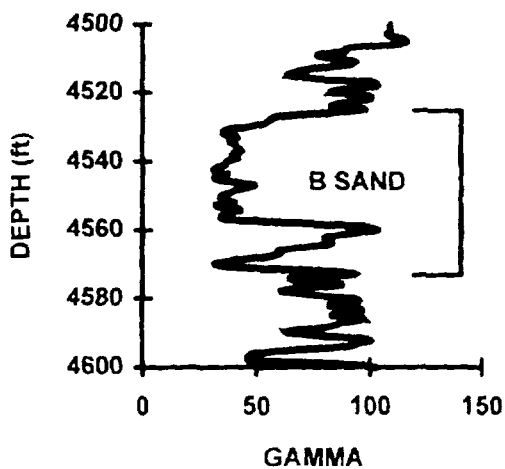


Figure 2. Gamma ray log showing B sand lithology

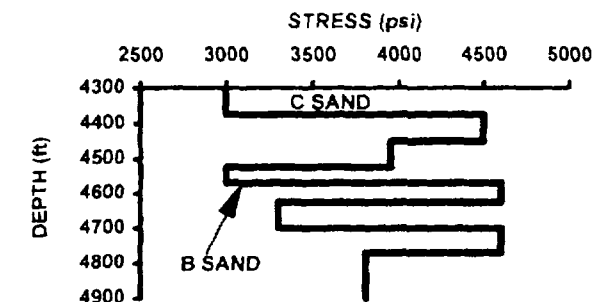
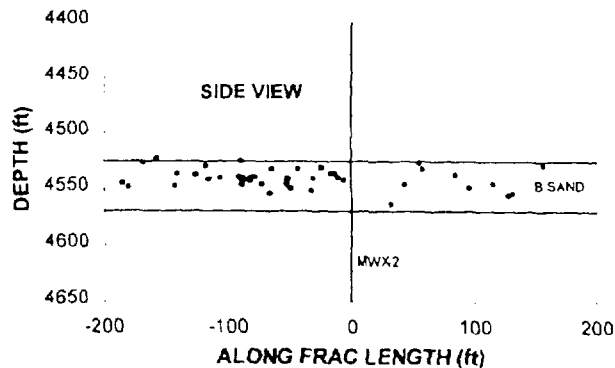


Figure 3. Stress contrasts around B sandstone

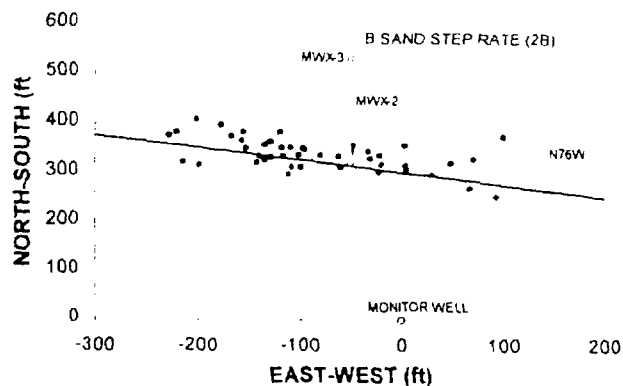


Figure 5. Microseismic images of fracture 2B

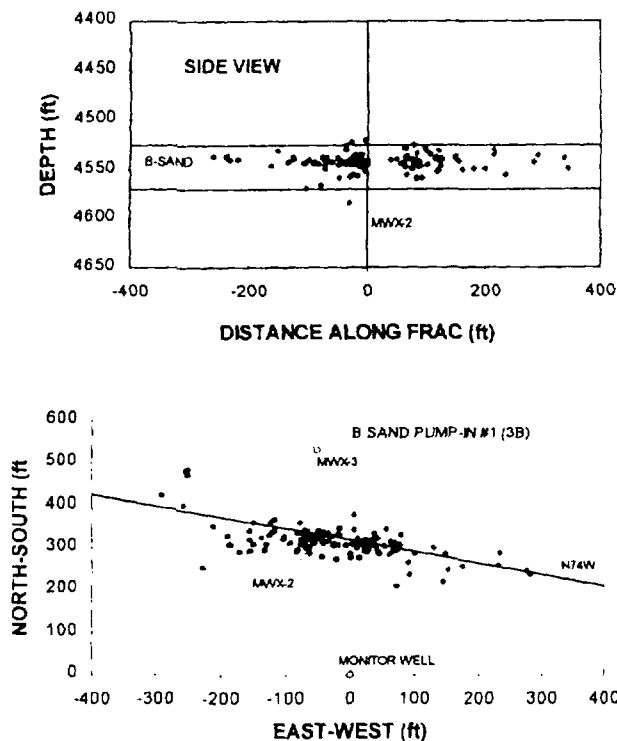


Figure 6. Microseismic images of Fracture 3B

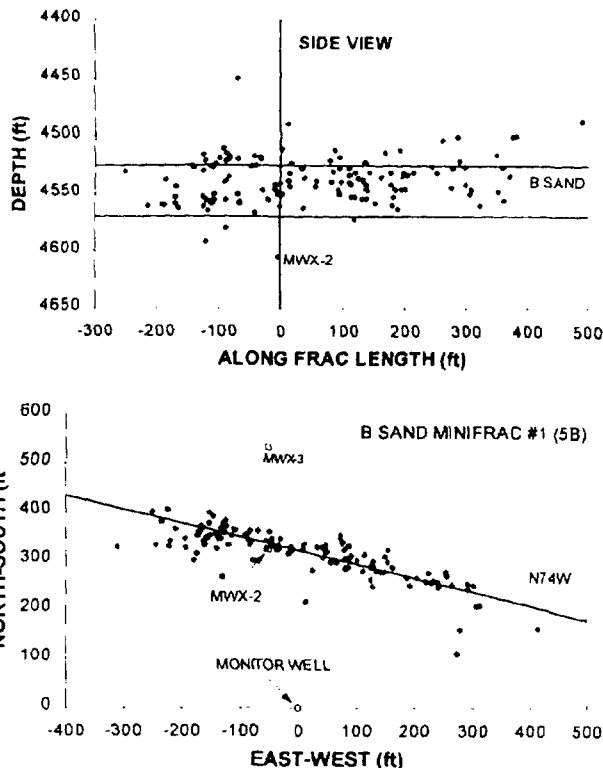


Figure 8. Microseismic images of fracture 5B

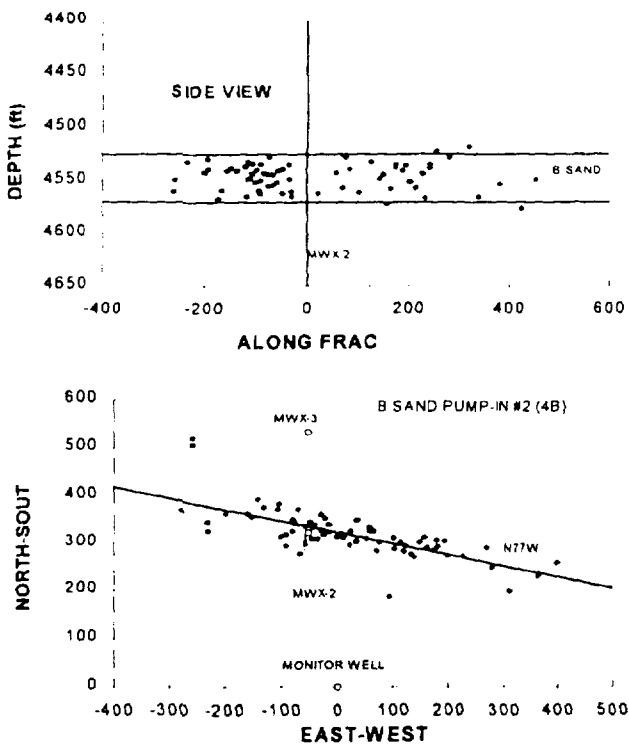


Figure 7. Microseismic images of fracture 4B

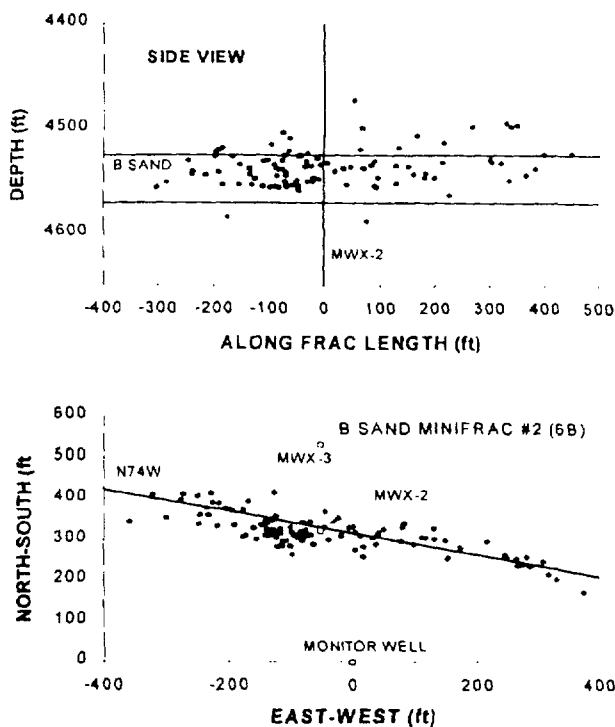


Figure 9. Microseismic images of fracture 6B

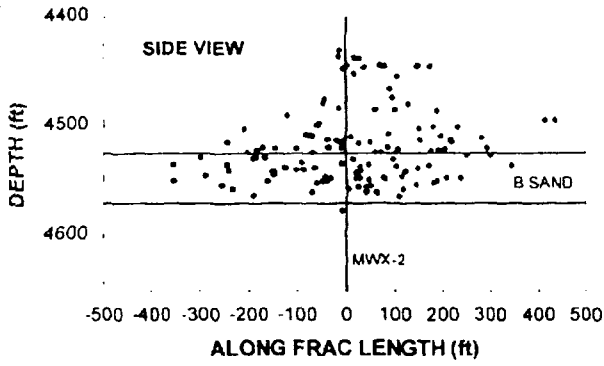


Figure 10. Microseismic images of fracture 7B

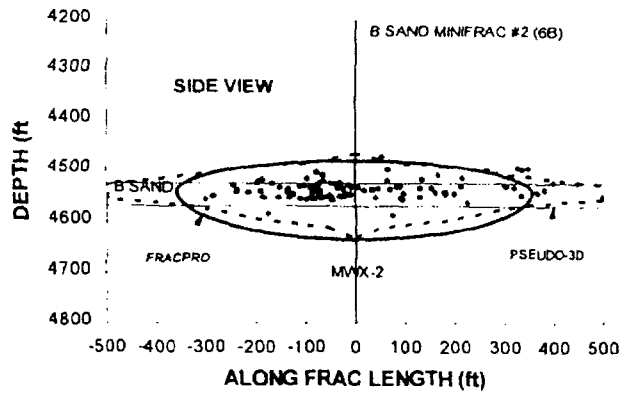


Figure 11. Comparison of models with fracture 4B image

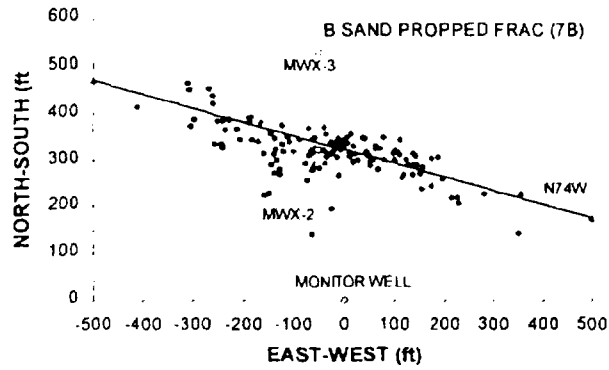


Figure 12. Comparison of models with fracture 6B image

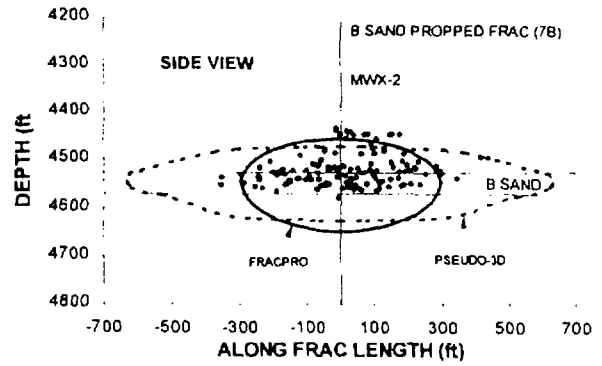


Figure 13. Comparison of models with fracture 7B image

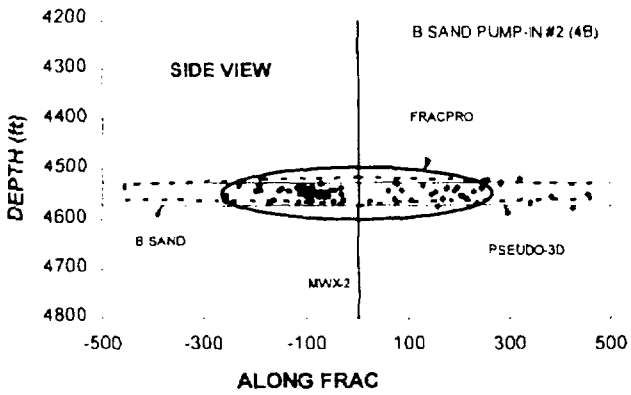


Figure 14. Comparison of models with fracture 4B image